Title: A nucleation distance sets the cell size-dependent P-body assembly

Authors: Xuefang Gu[1], Dexin Shen[1], Xing Quan[1], Tatsuhisa Tsuboi[1, *]

Affiliations:

[1] Institute of Biopharmaceutical and Health Engineering, Tsinghua Shenzhen International Graduate School, Shenzhen 518055, China

*To whom correspondence should be addressed:

Tatsuhisa Tsuboi

Institute of Biopharmaceutical and Health Engineering, Tsinghua Shenzhen International Graduate School, Shenzhen 518055, China

Tel: +86-152-1679-5216

E-mail address: ttsuboi@sz.tsinghua.edu.cn

Abstract:

Cells rely on diverse intracellular structures, including phase-separated granules, to regulate biological processes. Processing body (P-body) is a type of membraneless condensate in the eukaryotic cytoplasm that mediates mRNA degradation and storage. While their molecular composition is well studied, the relationship between their spatial organization and cell geometry, particularly cell size and organelle distribution, remains unclear. Here, we develop a conceptual framework that models phase-separation nucleation and validates the nucleation distance of P-bodies in living yeast cells. Using microfluidic cell sorting and quantitative fluorescence microscopy, we find that small cells contain fewer but larger P-bodies, whereas large cells form more but smaller granules. Monte Carlo simulations of P-body nucleation accurately recapitulate these cell size-dependent patterns and reveal a nucleation distance of 2.2 μm. Furthermore, we demonstrate that increasing vacuolar volume reduces the effective cytoplasmic space and correspondingly raises P-body number, although cell size remains the dominant determinant. Our findings establish nucleation distance as a key parameter that links cell geometry to the biophysical regulation of condensate formation.

Keywords

P-body, cell size, phase separation, modeling, microfluidics

Introduction

Cellular structures act in concert to regulate essential processes such as intracellular transport, energy conversion, and gene expression [1–3]. Among these structures, membrane-less organelles formed through liquid-liquid phase separation (LLPS) play a critical role in gene expression regulation [4–6]. Cytoplasmic Processing bodies (P-bodies) are prototypical LLPS condensates in eukaryotic cells [3]. They sequester translationally repressed messenger RNAs (mRNAs) together with the decapping and decay enzymes [7,8], thereby orchestrating mRNA degradation, storage, and recycling [8–11]. P-body assembly involves several partially redundant scaffold proteins, including Edc3[12,13], Dcp2[14], Dhh1 [15], Pat1 [15,16], and Lsm4 [12,17]. Deletion of these key proteins typically reduces P-body number and size and impairs the recruitment of client RNAs and proteins [18,19].

Phase separation begins with nucleation, the process in which a small molecular cluster becomes large enough to overcome the energetic cost of forming a new interface. In supersaturated solutions or vapours, only molecules that diffuse within a reaction radius can bind productively; beyond this distance, collisions are too infrequent to surpass the nucleation barrier [20]. Once a condensate forms, it recruits nearby molecules, creating a depletion zone that reduces local supersaturation. New droplets can only nucleate beyond this depleted region. Together with the natural tendency of neighboring droplets to fuse and minimize surface energy, this phenomenon defines a characteristic nucleation distance (d_n), the typical spacing at which independent condensates can stably coexist [21]. Inside cells, molecular crowding and sub-diffusive dynamics further limit droplet fusion, allowing many condensates to persist at approximately d_n apart rather than merging into a single large phase [22]. Simulations using a coarse-grained protein model reveal that the stability of biomolecular condensates depends mainly on the number of attractive interactions between

molecules [23]. By modulating concentration, crowding, or binding affinity, cells can tune d_n to control both the number and spatial distribution of condensates.

Despite the complexity of the intracellular environment, nucleation in living cells still adheres to fundamental physics constraints, the existence of an energy barrier, and the requirement for a critical molecular cluster, with cellular components often acting as seeds to facilitate this process [20]. The concept of a nucleation distance thus bridges physical theory and cell biology, as it arises from the necessity of accumulating sufficient molecules within a reaction radius and is reinforced by molecular depletion effects and coalescence dynamics, ultimately leading to a regulated, non-random spatial distribution of condensates within the cell. These insights suggest that P-body assembly is governed not only by protein composition and interactions but also by the physical dimensions and spatial organization of the cell.

Cellular organization is determined by the geometry of intracellular compartments and directly influences the scale and efficiency of biosynthetic processes [24–26]. As cells grow larger, organelles generally scale proportionally [27–29]. Although the total protein concentration is maintained, the concentration of individual proteins may increase or decrease with cell size [30–32]. Interestingly, P-bodies are known to appear during G1 and expand in size through G2, without a corresponding change in number [33], suggesting that spatial constraints, rather than protein abundance, may play a key role in phase separation. Yet, the precise influence of cell size and spatial parameters on P-body formation and dynamics remains largely unexplored.

80 Here, we extend this conceptual framework to quantitatively model condensate nucleation and
81 validate the presence of a characteristic nucleation distance in living cells. By combining
82 quantitative microscopy of size-sorted cells using microfluidic devices with Monte Carlo
83 simulations for nucleation, we find that larger cells tend to form more but smaller P-bodies,
84 whereas smaller cells generate fewer but larger P-bodies. The simulations identify a specific
85 nucleation distance (d_n) that aligns closely with our experimental observations. Moreover, in *sch9*Δ
86 and *vps1*Δ mutants, where vacuolar volume is enlarged and the effective cytoplasmic space
87 reduced, we observe a significant increase in P-body number, reinforcing the importance of spatial
88 restriction in phase separation. Together, these results enable us to investigate how cells regulate
89 the nucleation distance to influence the formation, size, and distribution of phase-separated
90 compartments.
91

92 **Results**

93 **P-body number increases with yeast cell size**

94 To examine the relationship between cell size and P-body formation under physiological
95 conditions, we quantify how the spatial organization and cell geometry of a yeast cell influence
96 the initiation and abundance of P-bodies *in vivo* while avoiding genetic manipulations that can
97 inadvertently perturb LLPS [34,35]. We developed a microfluidic device based on cell trapping for
98 long-term time-lapse microscopy [36,37], containing one hundred parallel trap lines whose
99 constriction widths increase stepwise from 5.1 µm to 10 µm, enabling continuous perfusion of
100 logarithmically growing W303 cells and deterministic physical sorting by diameter (Fig. 1A, B,
101 Supplementary Fig. 1). This non-invasive, high-throughput platform let us examine a wide range
102 of cell sizes in a single experiment while minimizing batch-to-batch variability (Supplementary

103 Fig. 1C). This platform preserved nutrient availability while imaging under an identical
104 glucose-starvation regime (0 % glucose, synthetic complete medium), a known physiological
105 stress that robustly induces P-body formation. The use of physical sorting rather than genetic
106 perturbation was essential to isolate the impact of cell size and to avoid confounding factors such
107 as stress responses, altered expression of phase-separation components, or cell-cycle defects.
108
109 We tagged Dcp2, a core P-body scaffold, with a newly engineered green fluorescent protein
110 variant, mAbbsinthe, which exhibits superior photostability and lower self-aggregation relative to
111 conventional GFPs (Supplementary Fig. 2A, B)[38]. Dcp2-mAbbsinthe retained its ability to induce
112 P-body formation in response to stress, confirming its suitability as a functional reporter
113 (Supplementary Fig. 2C). The enhanced photostability of mAbbsinthe was critical for long-term
114 imaging of condensate dynamics under glucose starvation. Using spinning-disk confocal
115 microscopy, we acquired three-dimensional stacks of P-body distribution in yeast cells spanning
116 the full diameter range (Fig. 1C). Quantitative analysis revealed a strong positive correlation
117 between cell size and p-body number (Fig. 1D). The mean P-body number per cell rose from 2.7
118 in 3.5–4.5 µm cells to 4.4 in 4.5-5.5 µm cells, and to 6.2 in cells larger than 5.5 µm. These findings
119 were reproduced with Edc3-mAbbsinthe, an alternative P-body marker, demonstrating that the
120 effect is not reporter-specific. Together, our results provide direct experimental evidence that cell
121 size is a key determinant of P-body number, suggesting that cellular geometry influences phase
122 separation behavior *in vivo*.
123
124 **A Monte-Carlo simulation based on nucleation identifies a characteristic nucleation distance**

125 To test whether simple geometric constraints could explain the empirically observed scaling, we
126 implemented a Monte-Carlo simulation based on nucleation. In this model, we approximated the
127 yeast mother cell as a sphere and randomly distributed virtual Dcp2 molecules within its volume
128 (Fig. 2A). This abstraction was motivated by the physical properties of phase-separated
129 condensates, which behave as mesoscale entities with restricted mobility and volume-excluding
130 effects. Collisions resulting in center-to-center separations below a tunable threshold (nucleation
131 distance, d_n) trigger irreversible coalescence, conserving total mass. These fusion events were
132 iteratively calculated until all remaining molecular pairs were spaced beyond this threshold. We
133 initialized the model with 200 seed spheres per cell, each with a radius of 2.0 to 3.0 µm. Across
134 this range, a best-fit d_n of 2.2 µm simultaneously reproduced the monotonic increase in puncta
135 number with cell size (Fig. 1D, 2B, Supplementary Figure 3A). We then compared the size of P-
136 bodies between simulations and experiments. Since P-bodies were visualized through microscopy
137 imaging, apparent measurements can deviate from actual biological sizes. To ensure consistent
138 comparison, we quantified P-body size by calculating the proportion of puncta in each size
139 category (Supplementary Figure 3B). We first matched the category proportion between the two
140 experiments for a cell size of 5.0 µm. With this size classification, the simulation for the other two
141 different size cells, 4.0 µm and 6.0 µm, matches surprisingly well with the empirically observed
142 triphasic size distribution of P-bodies (Fig. 2C - G). Smaller cells tend to form larger P-bodies,
143 whereas larger cells predominantly contain smaller P-bodies. This agreement suggests that the
144 physical spacing between successful nucleation events, a feature not encoded in protein sequence
145 or interaction affinity, acts as a central organizing principle. To probe robustness, we performed
146 sensitivity analyses that varied initial molecular numbers and cytoplasmic viscosity
147 (Supplementary Figure 3C, D). The final puncta number was largely invariant to particle count

148 above ~200 and only weakly dependent on viscosity (within biologically plausible ranges),
149 indicating that d_n is the dominant determinant of condensate distribution. These simulations
150 highlight that spatial constraints and collision thresholds alone are sufficient to explain the
151 observed morphological transitions, without invoking complex biochemical regulation.
152

153 **Organelle occupancy amplifies nucleation frequency by restricting effective cytoplasmic**
154 **volume**

155 While total cell volume increases during growth, the effective cytoplasmic space available for P-
156 body formation may be limited by the presence of large organelles such as the vacuole and nucleus.
157 To explore the impact of such intracellular crowding, we extended our simulation to incorporate
158 internal organelles occupying specific volumetric fractions. We implemented three distinct models
159 to simulate molecule fusion paths in the presence of a central spherical nucleus and vacuole,
160 representing non-permissive organelle space: (1) path-restricted fusion, in which straight-line
161 paths that crossed the nucleus were invalid, (2) path-shifted fusion, in which granules repositioned
162 to avoid organelle overlap, and (3) path-redirected fusion, in which particles navigated around
163 obstacles using a calculated shortest path (Fig. 3A–C).
164

165 Across all models, increasing organelle volume fractions consistently led to elevated final P-body
166 counts, even under a constant nucleation distance (Fig. 3D–G). This effect arose because internal
167 obstructions constrained the diffusion space, increasing local molecule concentrations and
168 reducing the effective reaction volume. These simulations suggest that intracellular crowding can
169 enhance condensate nucleation independent of changes in protein concentration or binding

170 affinity, highlighting a potential mechanism for tuning granule formation through organelle scaling
171 or spatial reorganization.
172
173 **Vacuole mutants validate the influence of spatial confinement on P-body assembly**
174 To test the simulation-derived hypothesis that intracellular crowding promotes condensate
175 nucleation, we examined two yeast mutants known to affect vacuolar morphology: *sch9*Δ and
176 *vps1*Δ. Both mutations increase vacuole-to-cell volume ratio through distinct mechanisms: *vps1*Δ
177 via impaired membrane fission and *sch9*Δ via defects in nutrient sensing and vacuolar growth
178 regulation [27,39]. Quantification of vacuole-to-cell volume ratios confirmed significantly increased
179 organelle occupancy in both mutants compared to wild-type (Fig. 4A, B). Fluorescence intensity
180 analysis showed that Dcp2-mabbsinthe expression remained unchanged (Fig. 4C), ensuring that
181 any observed effects on P-bodies were not due to altered protein abundance. As predicted by the
182 simulation, *vps1*Δ cells exhibited significantly higher P-body counts across all size bins (Fig. 4D),
183 indicating that reduced cytoplasmic space can elevate nucleation rates. Surprisingly, *sch9*Δ cells,
184 despite also showing increased vacuole volume, did not exhibit a similar rise in P-body number.
185 Instead, both *sch9*Δ and *vps1*Δ displayed a marked shift toward smaller P-body sizes (Fig. 4E, F),
186 especially in larger cells.
187
188 This discrepancy can be reconciled by considering the nonlinear relationship between volume and
189 linear distance: a 10% reduction in cytoplasmic volume translates to only about 3.45% shrinkage
190 in radius, equivalent to ~0.17 μm for a typical yeast cytoplasmic dimensions (~5 μm). This
191 reduction is minor compared to the ~2.2 μm nucleation distance inferred from simulations. Thus,
192 small changes in cytoplasmic diameter may be insufficient to affect nucleation probability, yet

193 they may impair granule coalescence, favoring fragmentation in *sch9*Δ cells. In addition, the
194 simulated puncta numbers correspond to a scenario in which the central sphere occupies less than
195 1% of the whole-cell volume, using a d_n of 2.2 μm, which is far below the actual occupation by
196 the organelles (Fig. 3D-F). This suggests that effective intervention by the cellular organization
197 must be much smaller, possibly due to the condensate itself, which diffuses within the cell. These
198 findings experimentally confirm that intracellular crowding affects P-body morphology and
199 support the existence of a spatially constrained fusion threshold that governs the organization of
200 condensates.
201

202 **Larger P-bodies exhibit delayed disassembly upon nutrient repletion**

203 Having established that spatial parameters regulate condensate number and size, we next asked
204 whether these morphological features influence functional stability. In classical phase-separation
205 systems, larger droplets are thermodynamically favored and dissolve more slowly due to reduced
206 surface-to-volume ratios and kinetic buffering [40]. We hypothesized that large P-bodies would
207 persist longer upon glucose reintroduction, providing a functional correlation to their size. We
208 performed time-lapse confocal imaging of glucose-starved cells subjected to nutrient repletion and
209 tracked P-body disassembly across a 10-minute window. As expected, small and medium P-bodies
210 disappeared rapidly, with more than 80% disassembling within four minutes (Fig. 5A–B). In
211 contrast, large P-bodies were highly stable, often persisting until the final time point. This size-
212 dependent disassembly rate suggests that larger condensates have altered material properties, such
213 as increased viscosity or reduced surface curvature, that slow their dissolution. These results
214 suggest that condensate size is not merely a geometric consequence of fusion events but has
215 functional implications for granule stability and cellular memory. Larger P-bodies may act as more

216 robust repositories for mRNA and protein complexes, potentially influencing translational
217 reactivation or RNA decay following stress relief. This observation supports a model in which P-
218 body size encodes distinct biophysical states, governed by nucleation and fusion history, and
219 modulated by spatial constraints during formation.
220

221 **Discussion**

222 Our quantitative imaging combined with microfluidic cell size sorting and Monte Carlo modeling
223 shows that phase-separated P-bodies follow a characteristic nucleation distance (~2.2 μm), which
224 determines their abundance as a function of overall cell diameter (Fig. 1, 2). By demonstrating that
225 a single geometric parameter is sufficient to recapitulate the full empirical relationship between
226 cell size and condensate number, we provide, to our knowledge, the first *in vivo* measurement of
227 a nucleation distance for any biomolecular condensate. This finding confirms long-standing
228 predictions from classical nucleation theory [20–23] and extends them to the crowded, heterogeneous
229 cytoplasm. Previous work has shown that many organelles scale with growth [24–29], but whether
230 equivalent principles govern LLPS compartments has been unclear. Our microfluidic approach
231 allowed us to modulate cell diameter without genetic perturbation or cell cycle arrest, cleanly
232 separating geometric from biochemical variables. The experiments showed larger cells
233 consistently accumulated more, but smaller P-bodies (Fig. 1D). The simulation showed that this
234 pattern naturally arises when nucleation events are prevented within d_n of an existing droplet: as
235 the cytoplasmic volume increases, the number of non-overlapping spheres of radius d_n roughly
236 increases with volume (Fig. 2A-C). These data argue that cells can modulate condensate
237 abundance passively, simply by growing. Our minimal model deliberately omits molecular
238 interactions, active transport, or cytoskeletal barriers, yet captures the essential statistics of P-body

239 distribution. This parsimonious view suggests that d_n signifies a fundamental effective reaction
240 radius that incorporates all microscopic determinants (multivalent interactions, crowding,
241 diffusivity) into a single mesoscale parameter. Future work can refine this framework by allowing
242 d_n to vary in response to environmental cues, post-translational modifications, or ATP levels,
243 ultimately enabling the quantitative prediction of condensate patterns from first principles.
244
245 Extending the model to include a central vacuole and nucleus showed that increasing internal
246 occupancy raises condensate number even at constant cell size (Fig. 3). The effect is conceptually
247 similar to the soft wall confinement used to promote vapour nucleation in microfluidic cavitation
248 chambers: reducing accessible volume raises the local supersaturation of phase separating
249 components and shortens the mean free path required to exceed the nucleation barrier. The *vps1*Δ
250 mutant, which has an enlarged vacuole, validated this prediction in vivo, exhibiting higher P-body
251 counts across all size bins (Fig. 4D). By contrast, *sch9*Δ increased vacuole volume but did not
252 change granule number, highlighting that modest reductions in linear distance (< 0.1 µm) are
253 negligible relative to d_n, yet still fragment larger condensates and bias the population towards
254 smaller droplets (Fig. 4E–F). Together, these observations position spatial confinement as a
255 tunable knob for condensate biogenesis, complementing known biochemical regulators such as
256 post-translational modifications or RNA scaffolding [9–12,14–18,41].
257
258 The strikingly slower dissolution of large P-bodies after glucose re-addition (Fig. 5) mirrors classic
259 Ostwald ripening behaviour, in which surface curvature drives exchange with the soluble pool.
260 Our data, therefore, suggest that the history of nucleation and fusion events leaves a lasting
261 physical imprint that regulates the lifetime of stress-induced mRNA repositories. A speculative

262 but attractive model is that large, stable granules favour selective retention of particular mRNAs
263 or protein complexes, endowing cells with a tunable memory of past stress episodes. P-bodies are
264 known to appear in G1 and grow through G2 without changing in number [33]. We reconcile this
265 observation with our findings by noting that budding yeast double their diameter only late in the
266 cell cycle; before this size threshold is crossed, the cytoplasm remains too small to permit
267 additional nucleation sites. More broadly, any physiological or pathological state that alters cell
268 volume or organelle allotment, such as hypertrophic growth, vacuolar fragmentation in aging, or
269 lysosomal enlargement in neurodegeneration, could reshuffle the cellular condensate landscape.
270 Indeed, impaired clearance of RNA granules is implicated in ALS and related disorders [6]. We
271 propose that disrupted spatial scaling, rather than intrinsic changes in phase-separating proteins,
272 may contribute to the aberrant accumulation of condensates in these contexts.
273
274 We imposed glucose starvation to synchronize P-body formation; whether d_n is conserved for other
275 stresses or constitutive granules, such as stress granules, remains to be tested. Additionally, the
276 model treats cells as perfect spheres and neglects the geometry of buds or cytosolic viscosity
277 gradients. High-speed light sheet imaging of nascent granules could capture accurate nucleation
278 kinetics and refine these assumptions. Furthermore, our static snapshots cannot distinguish
279 between *de novo* nucleation and the fission of pre-existing droplets; combining selective
280 photoconversion with long-term tracking would resolve this issue. Finally, although we focused
281 on scaffold protein concentration, RNA itself can nucleate P-bodies [41]; incorporating measured
282 RNA fluxes may sharpen model accuracy. By quantitatively bridging cell-scale geometry with
283 mesoscale phase behaviour, our study uncovers a simple spatial rule that governs how many
284 condensates a cell can host. We anticipate that nucleation distance will prove to be a unifying

285 concept across diverse LLPS assemblies, offering a geometric lens through which to interpret the
286 dynamic self-organization of the cytoplasm.
287
288 **Methods**
289 **Yeast strains and plasmids**
290 The yeast strains and plasmids used are listed in Supplementary File 1, and the oligonucleotides
291 used for plasmid construction and gene modification are listed in Supplementary File 2. To reduce
292 variability among the constructed yeast strains, the strains were created either through the
293 integration of a linear PCR product or a plasmid linearized through restriction digestion. The
294 variants of yeast expression plasmids (TTP257, PXQP017) for fluorescent protein were
295 constructed by swapping GFP of pFA6a-link-yoGFP-SpHis5[42] with mAbb0.5 and mAbbsinthe[38]
296 through the combination of Gibson assembly and PCR. Fluorescent protein tagging for Dcp2 and
297 Edc3 with mAbb0.5, mAbbsinthe, and yoGFP was performed with PCR-mediated homologous
298 recombination using TTP257, PXQP017, and pFA6a-link-yoGFP-SpHis5, and integrations were
299 confirmed by microscopy. Su9-mCherry was expressed by the TDH3 promoter from the integrated
300 plasmid TTP076, and the strains with three copies of the integrated plasmids in a cell were
301 screened through microscopy and used for further experiments. Deletion mutant strains were
302 constructed with PCR-mediated homologous recombination using pFA6a-hphMX6, and the
303 integration of the hphMX6 cassette was confirmed by PCR followed by electrophoresis.
304
305 **Microfluidic device fabrication**

306 The design and fabrication of the microfluidic device for yeast replicative aging were based on
307 previously published work [43,44]. To enable the capture of yeast cells with different diameters, the
308 initial 6 µm cell trap design was adjusted to include trap diameters ranging from 5.1 to 10 µm.
309

310 **Setting up a microfluidic experiment**

311 Before the microfluidics experiment, the device was placed under vacuum for 20 minutes to
312 remove air from the channels. The device was then placed on the stage of an inverted spinning
313 disk confocal microscope. Media ports were connected to plastic tubing, which in turn was
314 connected to 20 mL syringes filled with fresh synthetic complete medium (SD) (CSM powder
315 from Sunrise Science, #1001-100, supplemented with 2% glucose and 0.04% Tween-20). These
316 syringes were positioned approximately 24 inches above the microscope stage to drive media flow
317 via gravity. Yeast cells were grown in SC medium at 30℃ with a rotator speed of 70 rpm until
318 they reached an OD_{600} of approximately 1.0. The following day, yeast cells were diluted to an
319 OD_{600} of 0.1 and cultured for an additional 4 to 5 hours until they reached an OD_{600} of
320 approximately 0.6, before being used in the experiment. To capture the cells in the microfluidic
321 device, the culture was diluted 4-fold and transferred into a 20 mL syringe prefilled with fresh SC
322 medium containing 0.04% Tween-20. The media syringe was replaced with the syringe containing
323 the yeast culture temporarily for loading cells. Medium flow into the device was gravity-driven,
324 allowing cells to enter and occupy the traps. After loading, the yeast culture syringe was replaced
325 with the media supply syringe, and all tubing heights were adjusted to maintain a height differential
326 of approximately 60 inches.
327

328 **Microscopy**

329 Cells were imaged at 30℃ by an Eclipse Ti2-E Spinning Disk Confocal with Yokogawa CSU-X1
330 (Yokogawa) with 50 μm pinholes, located at the Tsinghua-SIGS Tsuboi Laboratory. Imaging was
331 performed using a CFI Plan Apochromat Lambda 100x 1.49 NA oil objective. Z-stacks (300nm
332 steps) were acquired by a Prime 95B sCMOS camera (Photometrics) (pixel size 0.11μm). Imaging
333 was controlled using NIS-Elements software (Nikon). Images of the microfluidic device were
334 acquired using the large-image acquisition mode. The scanning area was set to 0.1 × 1.5 mm with
335 a 10% overlap between adjacent fields.
336 A P-body visualization experiment in a 96-well plate was performed as follows: Yeast cells were
337 grown in SC medium with 2% glucose at 30°C with a rotator speed of 70 rpm. 100μl of mid-log
338 phase yeast cells (OD600 of 0.4 to 0.7) were harvested and placed into a 96-well Glass Bottom
339 Plate (Cellvis LLC) coated with 0.1 mg/mL concanavalin A (Sigma-Aldrich C2010). After 15
340 minutes of incubation, the well was washed twice with 100 μL of SC media without glucose and
341 then filled with 100 μL of SC media without glucose.
342
343 **The measurement of the photobleach resistance**
344 To measure the photobleach resistance of GFPs, a 488 nm laser and a 510–520 nm emission filters
345 were used. The cells were imaged with 50% of pre-set laser power 20 times. 25 frames of the z-
346 section with a 100-millisecond exposure time were acquired in steps of 300 nm. After background
347 subtraction, the total fluorescence intensity was divided by the cell occupation area in the image.
348 The fluorescence intensity was normalized to the initial intensity to obtain Relative Fluorescence
349 Strength (RFS). The average RFS of the 30 cells was calculated, and the RFS curve was created
350 by MATLAB (version 2021a) using polynomial curve fitting.
351

352 **Molecular nucleation model for P-body formation**

353 The model was based on a Monte Carlo simulation approach. Since the yeast cell is approximately
354 spherical, it was modeled as a spherical region in the simulation. P-bodies are randomly distributed
355 in the cytoplasm and are also roughly spherical; therefore, in the simulation, they were also defined
356 as spherical molecules. Details were as follows:

357

358 First, the initial number of molecules per cell and the number of simulated cells were defined. Cell
359 diameter was used to represent different cell sizes. In each simulation, the initial position and
360 volume of each molecule were assigned using a random number generator, and their positions
361 were marked in a three-dimensional Cartesian coordinate system. The following procedure was
362 employed to generate the three-dimensional coordinates for each molecule:

363 (1) Random angle generation: Two angles, θ and φ, representing the azimuthal and polar angles in
364 spherical coordinates, were generated using uniform random distributions.

365 (2) Radial distribution: A radial coordinate was calculated based on the predefined cell radius, with
366 a cube root distribution applied to ensure uniform volume distribution.

367 (3) Position conversion: Using the standard spherical-to-Cartesian coordinate transformation, the
368 position in spherical coordinates was converted to three-dimensional Cartesian coordinates
369 according to the following equations:

370 $$x = r * cos(\theta) * sin\,(\varphi)$$

371 $$y = r * sin(\theta) * sin\,(\varphi)$$

372 $$z = r * cos\,(\varphi)$$

373 Since this study induced P-body formation by applying glucose starvation stress, the mobility of
374 P-bodies in this condition is very slow and can be neglected [45]; therefore, the molecules were

375 considered to be in a static state. When the distance between two molecules fell below a critical
376 threshold (a predefined nucleation distance), these molecules were assumed to aggregate to
377 become one molecule.
378
379 The aggregation process was implemented as follows:
380 (1) Distance calculation and collision detection: To efficiently identify the closest pair of
381 molecules, an auxiliary function, *findclosestpoint*, was developed. Different models use different
382 *findclosestpoint* functions, as mentioned in Figure 3.
383 (2) Molecule merging: Upon collision, the volumes and positions of the two molecules were
384 merged. The resulting molecule had an increased volume, and its position was determined by
385 *findclosestpoint*.
386 (3) State update: The number and positions of molecules in the cell were updated accordingly after
387 each aggregation event.
388 The code updated the distribution of molecules in the cell based on the current positions and
389 volumes at each simulation step, progressively approaching the final aggregation state. The
390 simulation loop was terminated once the distances between all molecules exceeded the predefined
391 nucleation distance.
392
393 **Quantification and statistical analysis**
394 Detailed statistics, including the number of cells analyzed, mean value, standard deviation, and
395 standard error of the mean, are indicated in each figure legend. The Wilcoxon rank-sum test was
396 performed using GraphPad Prism (GraphPad software).
397
398 **Data and materials availability**

All data supporting the findings of this study are available within the paper and its supplementary information. Yeast strains and plasmids used in the study are provided in Supplementary File 1. The oligonucleotides used are listed in Supplementary File 2. Further information and requests for raw data and reagents should be directed to and will be fulfilled by the lead contact, T.T. (ttsuboi@sz.tsinghua.edu.cn).

Code Availability

The Pytorch codes for p-body drug screening can be found at https://github.com/xuexuegu/nucleation.git.

Supplemental information

Supplementary File 1 | List of yeast strains and plasmids

Supplementary File 2 | List of oligonucleotides

Acknowledgments

We thank members of the Tsuboi laboratory, especially Abdul Haseeb Khan, for helpful discussions and feedback on the paper. We thank Nathan Shaner and Gerard Lambert for sharing mAbb0.5 and mAbbsinthe plasmids and Nan Hao for sharing the design of the microfluidic device. This work was supported in part by the Key Research and Development Program of the Ministry of Science and Technology 2024YFE0102700, 2023YFA0914303, Shenzhen Science and Technology Innovation Commission WDZC20220811144737001, startup fund OD2021031C, Interdisciplinary Research and Innovation Fund JC2022008, and Overseas Research Cooperation Fund HW2024009 from Tsinghua SIGS (to T.T.),

Author contributions

X.G. and T.T. conceived and designed the project. X.G. and X.Q. performed wet experiments and analyzed image data. X.G. and D.S. performed image quantification and computational analysis. X.G. and T.T. wrote the manuscript.

Competing interests

The authors declare no competing interests.

References

1. van Bergeijk, P., Hoogenraad, C.C., and Kapitein, L.C. (2016). Right Time, Right Place: Probing the Functions of Organelle Positioning. Trends Cell Biol *26*, 121–134. https://doi.org/10.1016/j.tcb.2015.10.001.

2. Teti, A. (1992). Regulation of cellular functions by extracellular matrix. Journal of the American Society of Nephrology *2*, S83. https://doi.org/10.1681/ASN.V210s83.

3. Luo, Y., Na, Z., and Slavoff, S.A. (2018). P-Bodies: Composition, Properties, and Functions. Biochemistry *57*, 2424–2431. https://doi.org/10.1021/acs.biochem.7b01162.

4. West, A.P., and Shadel, G.S. (2017). Mitochondrial DNA in innate immune responses and inflammatory pathology. Nat Rev Immunol *17*, 363–375. https://doi.org/10.1038/nri.2017.21.

5. Ow, Y.-L.P., Green, D.R., Hao, Z., and Mak, T.W. (2008). Cytochrome c: functions beyond respiration. Nat Rev Mol Cell Biol *9*, 532–542. https://doi.org/10.1038/nrm2434.

6. Wang, B., Zhang, L., Dai, T., Qin, Z., Lu, H., Zhang, L., and Zhou, F. (2021). Liquid–liquid phase separation in human health and diseases. Signal Transduct Target Ther *6*, 290. https://doi.org/10.1038/s41392-021-00678-1.

7. Choi, Y.-J., and Song, K. (2022). Nst1, Densely Associated to P-Body in the Post-Exponential Phases of Saccharomyces cerevisiae, Shows an Intrinsic Potential of Producing Liquid-Like Condensates of P-Body Components in Cells. Int J Mol Sci *23*, 2501. https://doi.org/10.3390/ijms23052501.

8. Noda, N.N., Wang, Z., and Zhang, H. (2020). Liquid–liquid phase separation in autophagy. Journal of Cell Biology *219*. https://doi.org/10.1083/jcb.202004062.

9. Parker, R., and Sheth, U. (2007). P Bodies and the Control of mRNA Translation and Degradation. Mol Cell *25*, 635–646. https://doi.org/10.1016/j.molcel.2007.02.011.

10. Eulalio, A., Behm-Ansmant, I., and Izaurralde, E. (2007). P bodies: at the crossroads of post-transcriptional pathways. Nat Rev Mol Cell Biol *8*, 9–22. https://doi.org/10.1038/nrm2080.

11. Decker, C.J., and Parker, R. (2012). P-Bodies and Stress Granules: Possible Roles in the Control of Translation and mRNA Degradation. Cold Spring Harb Perspect Biol *4*, a012286–a012286. https://doi.org/10.1101/cshperspect.a012286.

12. Decker, C.J., Teixeira, D., and Parker, R. (2007). Edc3p and a glutamine/asparagine-rich domain of Lsm4p function in processing body assembly in *Saccharomyces cerevisiae*. J Cell Biol *179*, 437–449. https://doi.org/10.1083/jcb.200704147.

13. Xing, W., Muhlrad, D., Parker, R., and Rosen, M.K. (2020). A quantitative inventory of yeast P body proteins reveals principles of composition and specificity. Elife *9*. https://doi.org/10.7554/eLife.56525.

14. van Dijk, E. (2002). Human Dcp2: a catalytically active mRNA decapping enzyme located in specific cytoplasmic structures. EMBO J *21*, 6915–6924. https://doi.org/10.1093/emboj/cdf678.

15. Hurto, R.L., and Hopper, A.K. (2011). P-body components, Dhh1 and Pat1, are involved in tRNA nuclear-cytoplasmic dynamics. RNA *17*, 912–924. https://doi.org/10.1261/rna.2558511.

469 16. Sachdev, R., Hondele, M., Linsenmeier, M., Vallotton, P., Mugler, C.F., Arosio, P., and Weis, K.
470 (2019). Pat1 promotes processing body assembly by enhancing the phase separation of the DEAD-
471 box ATPase Dhh1 and RNA. Elife *8*. https://doi.org/10.7554/eLife.41415.

472 17. INGELFINGER, D., ARNDT-JOVIN, D.J., LÜHRMANN, R., and ACHSEL, T. (2002). The
473 human LSm1-7 proteins colocalize with the mRNA-degrading enzymes Dcp1/2 and Xrn1 in
474 distinct cytoplasmic foci. RNA *8*, 1489–1501. https://doi.org/10.1017/S1355838202021726.

475 18. Rao, B.S., and Parker, R. (2017). Numerous interactions act redundantly to assemble a tunable size
476 of P bodies in *Saccharomyces cerevisiae*. Proceedings of the National Academy of Sciences *114*.
477 https://doi.org/10.1073/pnas.1712396114.

478 19. Teixeira, D., and Parker, R. (2007). Analysis of P-Body Assembly in *Saccharomyces cerevisiae*.
479 Mol Biol Cell *18*, 2274–2287. https://doi.org/10.1091/mbc.e07-03-0199.

480 20. Shimobayashi, S.F., Ronceray, P., Sanders, D.W., Haataja, M.P., and Brangwynne, C.P. (2021).
481 Nucleation landscape of biomolecular condensates. Nature *599*. https://doi.org/10.1038/s41586-
482 021-03905-5.

483 21. Shin, Y., Chang, Y.C., Lee, D.S.W., Berry, J., Sanders, D.W., Ronceray, P., Wingreen, N.S.,
484 Haataja, M., and Brangwynne, C.P. (2018). Liquid Nuclear Condensates Mechanically Sense and
485 Restructure the Genome. Cell *175*. https://doi.org/10.1016/j.cell.2018.10.057.

486 22. Lee, D.S.W., Choi, C.H., Sanders, D.W., Beckers, L., Riback, J.A., Brangwynne, C.P., and
487 Wingreen, N.S. (2023). Size distributions of intracellular condensates reflect competition between
488 coalescence and nucleation. Nat Phys *19*. https://doi.org/10.1038/s41567-022-01917-0.

489 23. Espinosa, J.R., Joseph, J.A., Sanchez-Burgos, I., Garaizar, A., Frenkel, D., and Collepardo-
490 Guevara, R. (2020). Liquid network connectivity regulates the stability and composition of
491 biomolecular condensates with many components. Proc Natl Acad Sci U S A *117*.
492 https://doi.org/10.1073/pnas.1917569117.

493 24. Schmoller, K.M., and Skotheim, J.M. (2015). The Biosynthetic Basis of Cell Size Control. Trends
494 Cell Biol *25*, 793–802. https://doi.org/10.1016/j.tcb.2015.10.006.

495 25. Goehring, N.W., and Hyman, A.A. (2012). Organelle Growth Control through Limiting Pools of
496 Cytoplasmic Components. Current Biology *22*, R330–R339.
497 https://doi.org/10.1016/j.cub.2012.03.046.

498 26. Chan, Y.-H.M., and Marshall, W.F. (2010). Scaling properties of cell and organelle size.
499 Organogenesis *6*, 88–96. https://doi.org/10.4161/org.6.2.11464.

500 27. Chan, Y.-H.M., and Marshall, W.F. (2014). Organelle Size Scaling of the Budding Yeast Vacuole
501 Is Tuned by Membrane Trafficking Rates. Biophys J *106*, 1986–1996.
502 https://doi.org/10.1016/j.bpj.2014.03.014.

503 28. Rafelski, S.M., Viana, M.P., Zhang, Y., Chan, Y.-H.M., Thorn, K.S., Yam, P., Fung, J.C., Li, H.,
504 Costa, L. da F., and Marshall, W.F. (2012). Mitochondrial Network Size Scaling in Budding
505 Yeast. Science (1979) *338*, 822–824. https://doi.org/10.1126/science.1225720.

506 29. Jorgensen, P., Edgington, N.P., Schneider, B.L., Rupeš, I., Tyers, M., and Futcher, B. (2007). The
507 Size of the Nucleus Increases as Yeast Cells Grow. Mol Biol Cell *18*, 3523–3532.
508 https://doi.org/10.1091/mbc.e06-10-0973.

509 30. Lanz, M.C., Zhang, S., Swaffer, M.P., Ziv, I., Götz, L.H., Kim, J., McCarthy, F., Jarosz, D.F.,
510 Elias, J.E., and Skotheim, J.M. (2024). Genome dilution by cell growth drives starvation-like
511 proteome remodeling in mammalian and yeast cells. Nat Struct Mol Biol *31*, 1859–1871.
512 https://doi.org/10.1038/s41594-024-01353-z.

513 31. Zhurinsky, J., Leonhard, K., Watt, S., Marguerat, S., Bähler, J., and Nurse, P. (2010). A
514 Coordinated Global Control over Cellular Transcription. Current Biology *20*, 2010–2015.
515 https://doi.org/10.1016/j.cub.2010.10.002.

516 32. Newman, J.R.S., Ghaemmaghami, S., Ihmels, J., Breslow, D.K., Noble, M., DeRisi, J.L., and
517 Weissman, J.S. (2006). Single-cell proteomic analysis of S. cerevisiae reveals the architecture of
518 biological noise. Nature *441*, 840–846. https://doi.org/10.1038/nature04785.

519 33. Safieddine, A., Benassy, M.-N., Bonte, T., Slimani, F., Pourcelot, O., Kress, M., Ernoult-Lange,
520 M., Courel, M., Coleno, E., Imbert, A., et al. (2024). Cell-cycle-dependent mRNA localization in
521 P-bodies. Mol Cell *84*, 4191-4208.e7. https://doi.org/10.1016/j.molcel.2024.09.011.

522 34. Harvey, S.L., Enciso, G., Dephoure, N., Gygi, S.P., Gunawardena, J., and Kellogg, D.R. (2011). A
523 phosphatase threshold sets the level of Cdk1 activity in early mitosis in budding yeast. Mol Biol
524 Cell *22*, 3595–3608. https://doi.org/10.1091/mbc.e11-04-0340.

525 35. Jorgensen, P., Nishikawa, J.L., Breitkreutz, B.-J., and Tyers, M. (2002). Systematic Identification
526 of Pathways That Couple Cell Growth and Division in Yeast. Science (1979) *297*, 395–400.
527 https://doi.org/10.1126/science.1070850.

528 36. Li, Y., Jiang, Y., Paxman, J., O'Laughlin, R., Klepin, S., Zhu, Y., Pillus, L., Tsimring, L.S., Hasty,
529 J., and Hao, N. (2020). A programmable fate decision landscape underlies single-cell aging in
530 yeast. Science (1979) *369*, 325–329. https://doi.org/10.1126/SCIENCE.AAX9552.

531 37. Zhou, Z., Liu, Y., Feng, Y., Klepin, S., Tsimring, L.S., Pillus, L., Hasty, J., and Hao, N. (2023).
532 Engineering longevity - design of a synthetic gene oscillator to slow cellular aging. Science (1979)
533 *380*. https://doi.org/10.1126/science.add7631.

534 38. Lambert, G.G., Depernet, H., Gotthard, G., Schultz, D.T., Navizet, I., Lambert, T., Adams, S.R.,
535 Torreblanca-Zanca, A., Chu, M., Bindels, D.S., et al. (2020). Aequorea's secrets revealed: New
536 fluorescent proteins with unique properties for bioimaging and biosensing. PLoS Biol *18*,
537 e3000936. https://doi.org/10.1371/journal.pbio.3000936.

538 39. Tsuboi, T., Viana, M.P., Xu, F., Yu, J., Chanchani, R., Arceo, X.G., Tutucci, E., Choi, J., Chen,
539 Y.S., Singer, R.H., et al. (2020). Mitochondrial volume fraction and translation duration impact
540 mitochondrial mRNA localization and protein synthesis. Elife *9*.
541 https://doi.org/10.7554/eLife.57814.

542 40. Ostwald ripening (2014). In The IUPAC Compendium of Chemical Terminology (International
543 Union of Pure and Applied Chemistry (IUPAC)). https://doi.org/10.1351/goldbook.O04348.

544 41. Xing, W., Muhlrad, D., Parker, R., and Rosen, M.K. (2020). A quantitative inventory of yeast P
545 body proteins reveals principles of composition and specificity. Elife *9*.
546 https://doi.org/10.7554/eLife.56525.

547 42. Lee, S., Lim, W.A., and Thorn, K.S. (2013). Improved Blue, Green, and Red Fluorescent Protein
548 Tagging Vectors for S. cerevisiae. PLoS One *8*, e67902.
549 https://doi.org/10.1371/journal.pone.0067902.

550 43. Li, Y., Jiang, Y., Paxman, J., O'laughlin, R., Klepin, S., Zhu, Y., Pillus, L., Tsimring, L.S., Hasty,
551 J., and Hao, N. A programmable fate decision landscape underlies single-cell aging in yeast.

552 44. Paxman, J., Zhou, Z., O'Laughlin, R., Liu, Y., Li, Y., Tian, W., Su, H., Jiang, Y., Holness, S.E.,
553 Stasiowski, E., et al. (2022). Age-dependent aggregation of ribosomal RNA-binding proteins links
554 deterioration in chromatin stability with challenges to proteostasis. Elife *11*.
555 https://doi.org/10.7554/eLife.75978.

556 45. Joyner, R.P., Tang, J.H., Helenius, J., Dultz, E., Brune, C., Holt, L.J., Huet, S., Müller, D.J., and
557 Weis, K. (2016). A glucose-starvation response regulates the diffusion of macromolecules. Elife *5*.
558 https://doi.org/10.7554/eLife.09376.

559

560

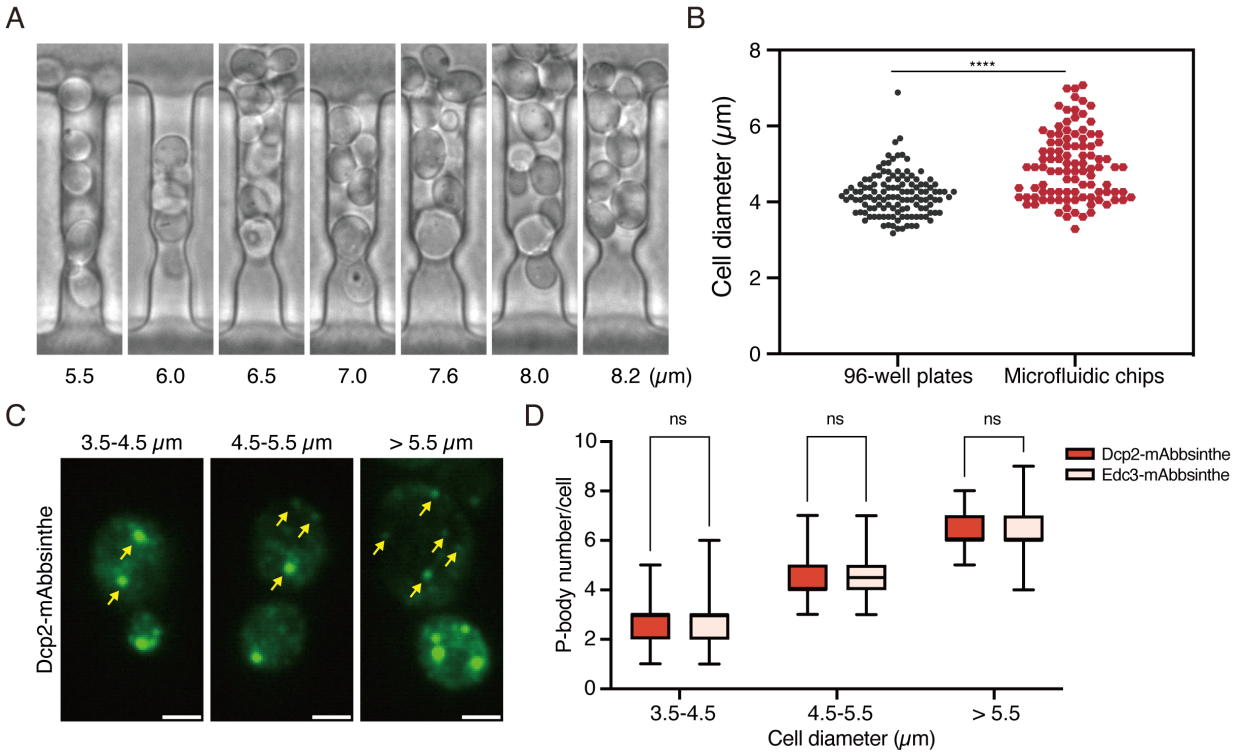

Figure 1 | P-body number increases with increasing yeast cell size

(A) Yeast cells of different sizes are captured in the microfluidic device; trap widths are indicated below each channel.

(B) Comparison of cell diameters in 96-well plates and microfluidic chips. Each dot corresponds to a single cell (n>90). Statistical significance was assessed by the Unpaired T-test (**** $P < 0.0001$).

(C) P-bodies in varying sizes of yeast cells were labeled with Dcp2-mAbbsinthe and analyzed 30 minutes after glucose starvation. Yellow arrows indicate P-bodies in mother cells. Scale bar, 2 µm.

(D) P-body number per cell across different cell sizes. Yeast cells expressing Dcp2-mAbbsinthe or Edc3-mAbbsinthe were categorized into three size ranges based on cell diameter. Statistical significance was assessed by Unpaired T-test (ns $P > 0.05$, n>30).

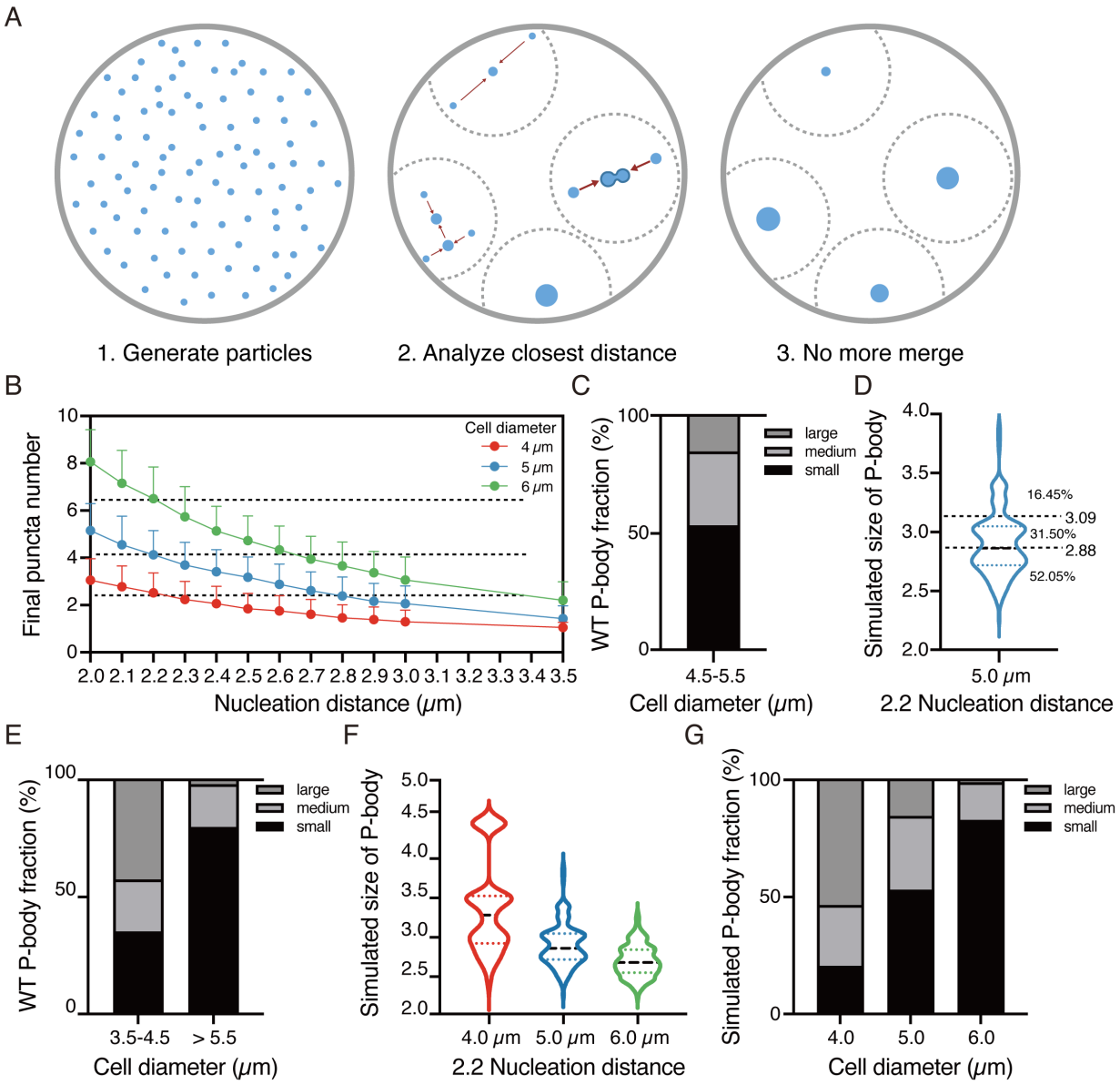

Figure 2 | A Monte-Carlo simulation based on nucleation identifies a characteristic nucleation distance

(A) Schematic representation of particle nucleation model based on Monte Carlo simulation. 1. Generate particles: Initial distribution of molecules in 3D space before simulation, each blue dot represents a molecule. 2. Analyze the closest distance: Each molecule recognizes the closest one and then fuses. 3. No more merge: Result of the nucleation model, showing puncta left after merge, each granule represents a P-body.

582 (B) Nucleation distance correlates with the final puncta number. Based on the nucleation distance,
583 final puncta numbers were simulated for each cell size (n = 200 per condition). Horizontal dashed
584 lines indicate the mean P-body number per cell of different cell size groups in Figure 1D.
585 (C) Size fraction of P-body in the 4.5-5.5μm cell size by the manual classification of the
586 microscope image.
587 (D) The definition of the size of the simulated P-bodies. The boundary for different sizes of P-
588 bodies in the simulation is based on the fraction in C.
589 (E) Size fraction of P-body in the different cell sizes by the manual classification of microscope
590 image data.
591 (F) Size of P-bodies in different cell sizes at the d_n = 2.2 μm in the simulation, including D.
592 (G) Fractions of the simulated P-body size in the different cell sizes based on the definition in D.
593

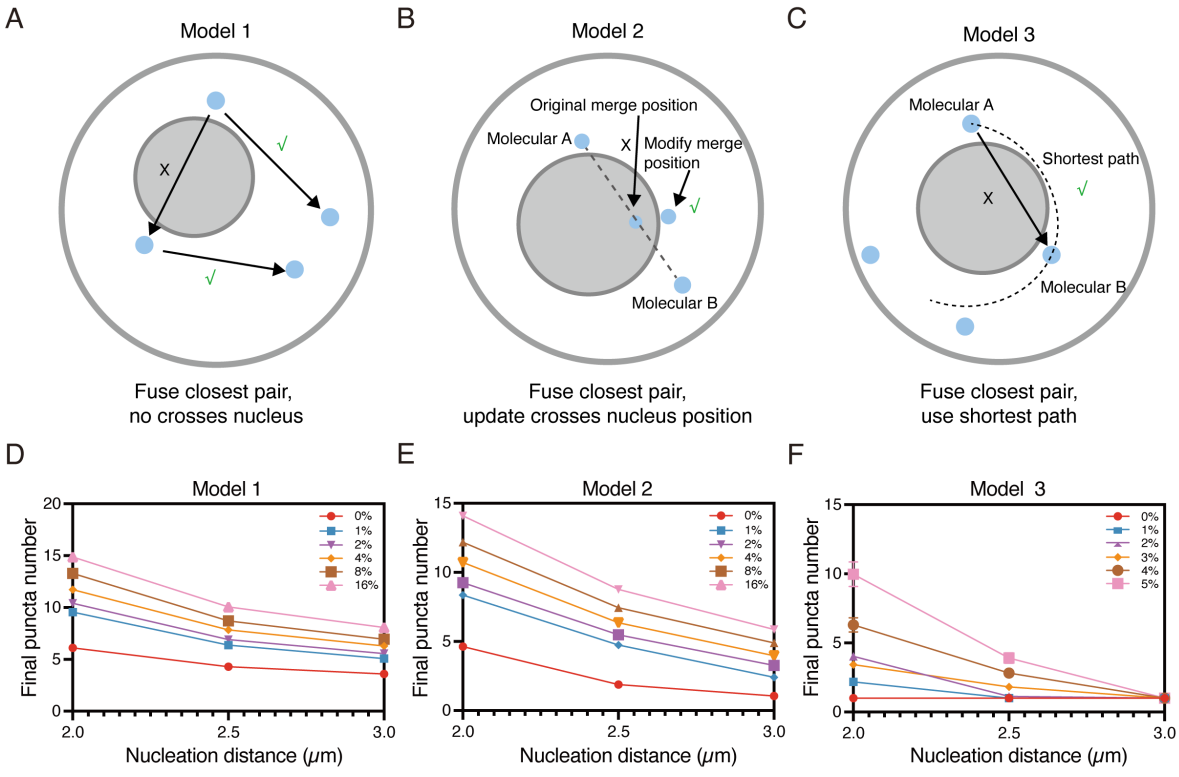

Figure 3 | Organelle occupancy amplifies nucleation frequency by restricting effective cytoplasmic volume

(A-C) Schematic diagrams of three nucleation models in a cell containing a centrally located organelle (gray circle). The symbols "X" and "√" show whether a selected fusion path is valid based on each model's rules. "X" indicates it is not allowed, while "√" signifies it is permitted.

(A) Model 1: Molecules fuse with their closest neighbor only if the connecting line does not intersect the central organelle.

(B) Model 2: Molecules fuse with their closest neighbor even if the direct path crosses the nucleus, but the merged granule is repositioned to avoid overlap with the central organelle.

(C) Model 3: Molecules fuse with their closest neighbor based on the true shortest path around the nucleus, allowing nucleus-aware trajectories.

(D-F) Final puncta number as a function of nucleation distance and organelle volume fraction. Color represents the different organelle fractions relative to the cell.

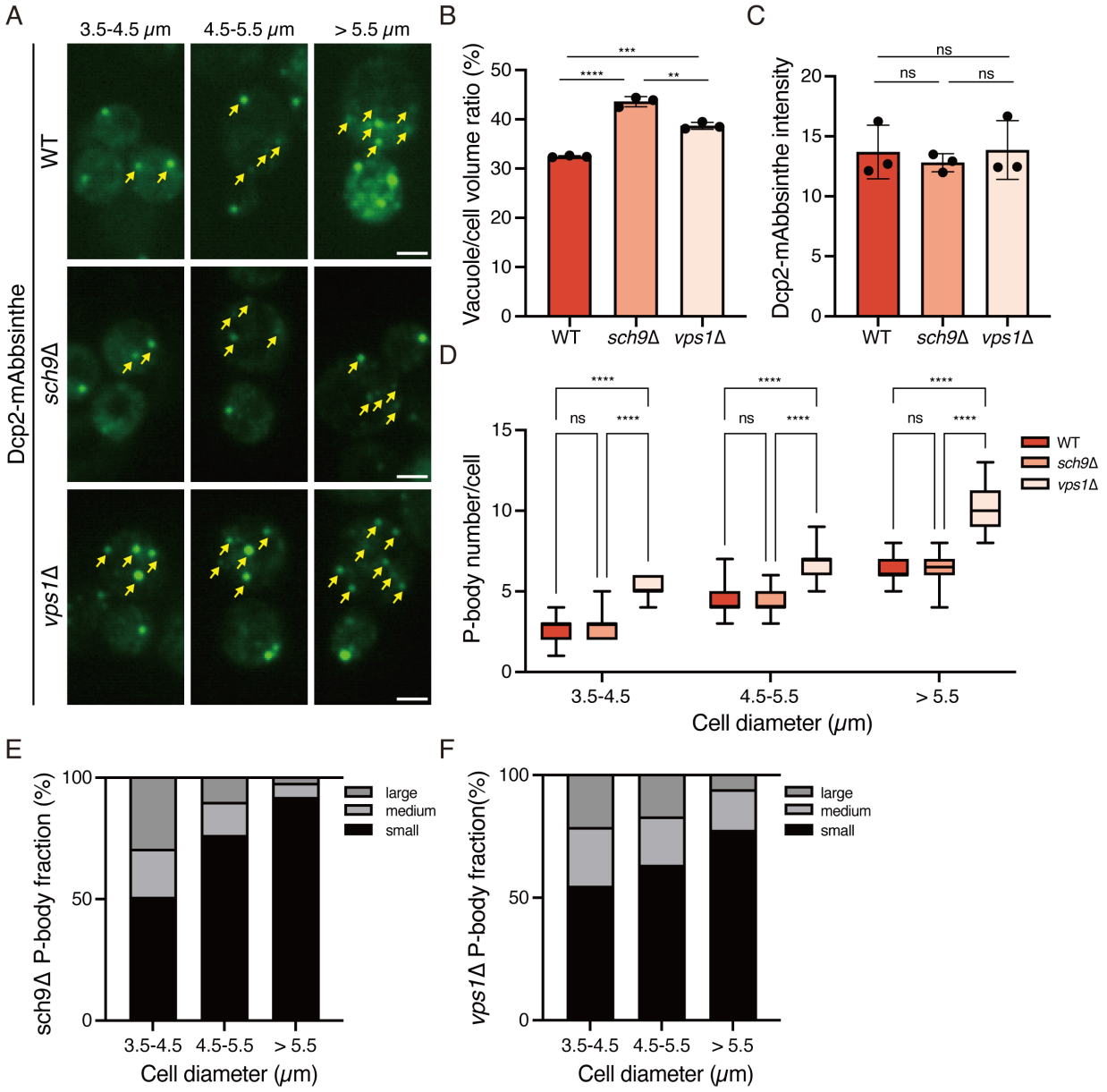

Figure 4 | Vacuole mutants validate the influence of spatial confinement on P-body assembly

(A) Visualization of P-bodies in WT, *sch9*Δ, and *vps1*Δ yeast strains expressing Dcp2-mAbbsinthe under glucose starvation for 30 minutes. Cells are grouped by cell diameter (3.5-4.5 µm, 4.5-5.5 µm, >5.5 µm), and P-bodies are indicated by arrows. Images are z-projections of 42 slices. Scale bar, 2 µm.

614 (B) Quantification of vacuole-to-cell volume ratio in WT, *sch9*Δ, and *vps1*Δ strains. Each dot
615 represents an individual experiment (n = 3 biological replicates). Statistical analysis was performed
616 using one-way ANOVA with multiple comparisons (**P < 0.01, ***P < 0.001, ****P < 0.0001).
617 (C) Mean Dcp2-mAbbsinthe fluorescence intensity in WT, *sch9*Δ, and *vps1*Δ strains. No
618 significant differences were observed. Each dot represents an individual experiment.
619 (D) P-body number per cell across different cell diameter groups (3.5-4.5 µm, 4.5-5.5 µm, >5.5
620 µm) in WT, *sch9*Δ, and *vps1*Δ strains. Statistical significance was determined by two-way
621 ANOVA with multiple comparisons (ns P > 0.05, ****P < 0.0001).
622 (E) Proportion of large, medium, and small P-bodies in *sch9*Δ cells across the cell size groups.
623 (F) Proportion of large, medium, and small P-bodies in *vps1*Δ cells across the cell size groups.
624

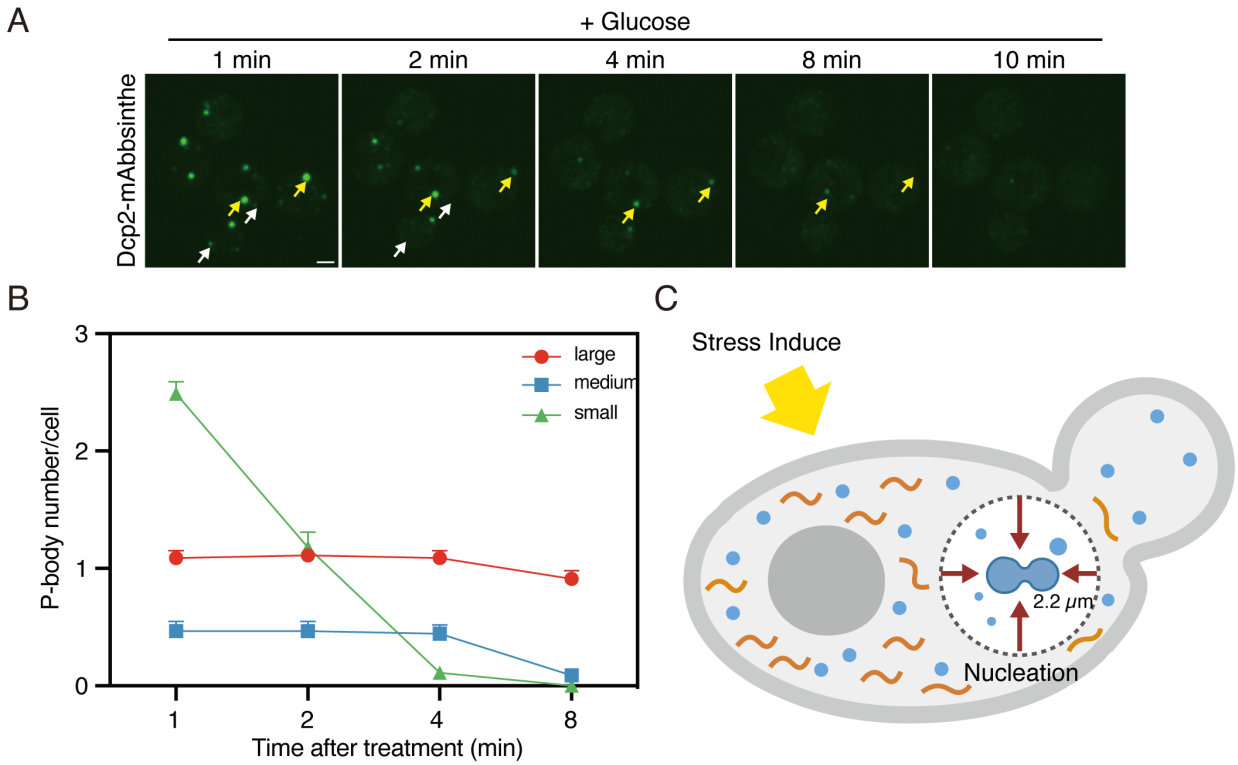

Figure 5 | Larger P-bodies exhibit delayed disassembly upon nutrient repletion

(A) Time-lapse images of P-bodies in yeast cells following glucose reintroduction after 30 minutes of starvation. Images were taken at 1, 2, 4, 8, and 10 minutes after the addition of glucose. Yellow arrows indicate large P-bodies, white arrows indicate small P-bodies. Images are z-projections of 42 slices. Scale bar, 2 µm.

(B) P-body numbers per cell over time after glucose reintroduction. Small P-bodies rapidly disaggregate, while large P-bodies remain stable. P-body size is primarily determined at the initial time point of formation. n> 45 cells within three independent experiments. Error bar represents s.e.m.

(C) Schematic model of P-body formation in yeast cells. Upon stress induction, molecular components (blue dots) and mRNA (orange lines) condense into P-bodies via nucleation within a spatial nucleation distance (~2.2 µm).

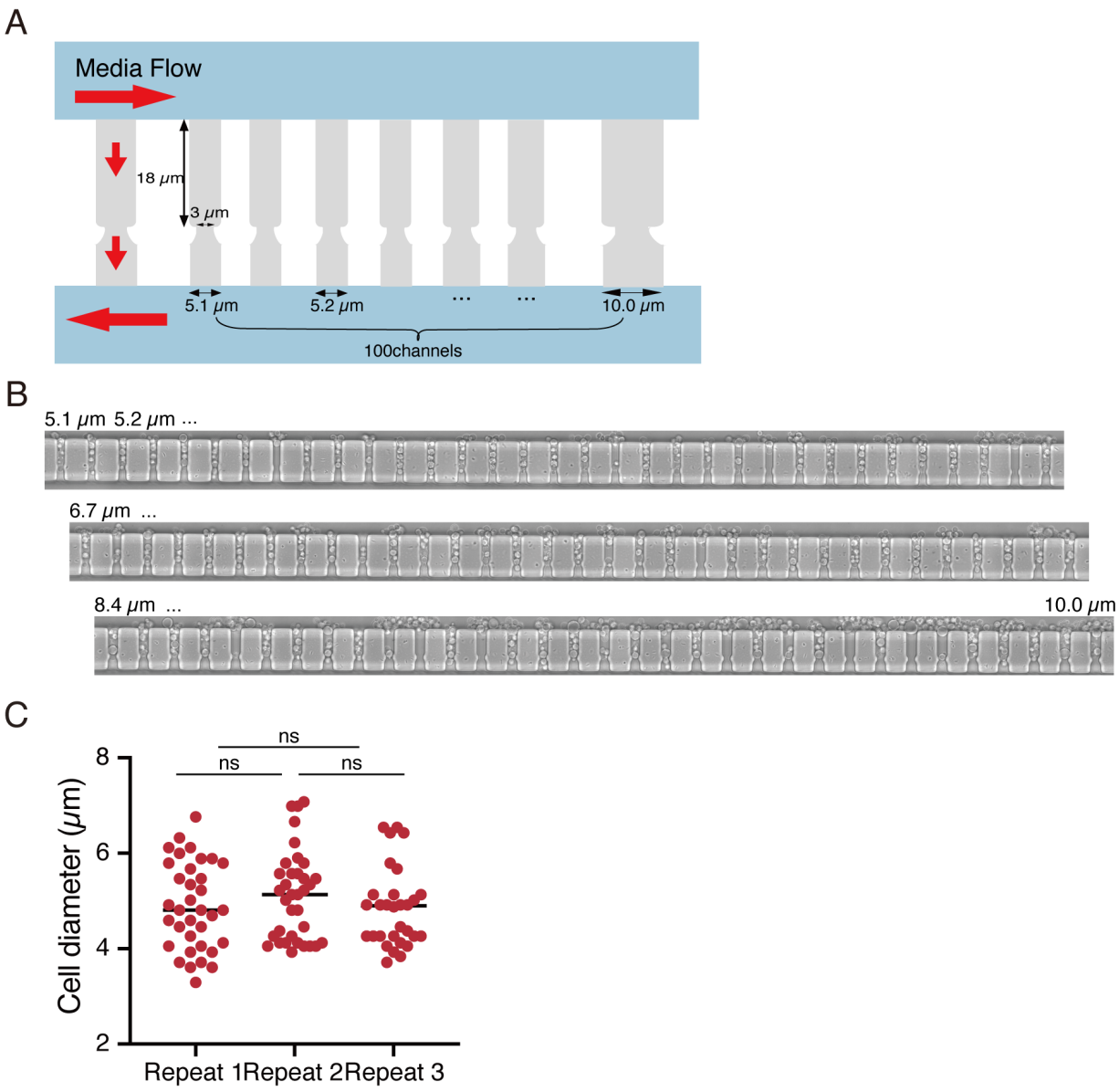

Supplementary Figure 1 | Design of microfluidics for different sizes of the cells

(A) Schematic design of the microfluidics device for capturing yeast cells of different sizes.

(B) Representative microfluidic device with a well size spanning 5.1 µm to 10 µm.

(C) The microfluidics consistently captures cells of different sizes (n ≥ 30 cells per repeat).

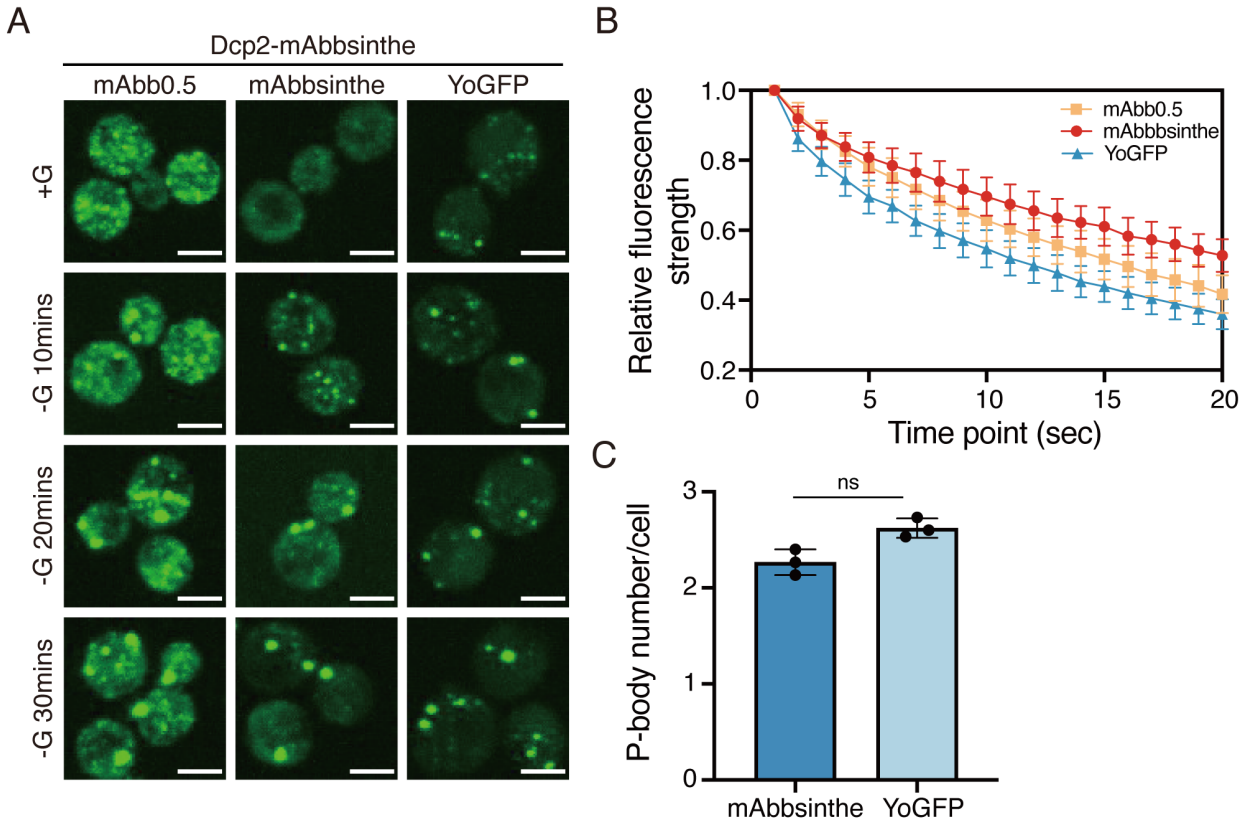

Supplementary Figure 2 | Dcp2 labeled with mAbbsinthe exhibits similar condensation and greater resistance to photobleaching compared to GFP

(A) Z-stack images of Dcp2 labeled with mAbb0.5, mAbbsinthe, and YoGFP. Cells were visualized during glucose (G) starvation at 0, 10, 20, and 30 minutes. All images share identical contrast settings. The scale bar indicates 2 µm.

(B) Various Dcp2-GFPs were photobleached under a 10-Watt laser for a 50-ms exposure for each time point. The fluorescence recovery was monitored for 20 seconds (n = 30 cells) and the relative fluorescence strength was plotted.

(C) P-body numbers per cell for mAbbsinthe and YoGFP-tagged Dcp2 after glucose starvation for 30 min. Statistical significance was assessed by the Unpaired T-test (ns $P > 0.05$, $n>30$).

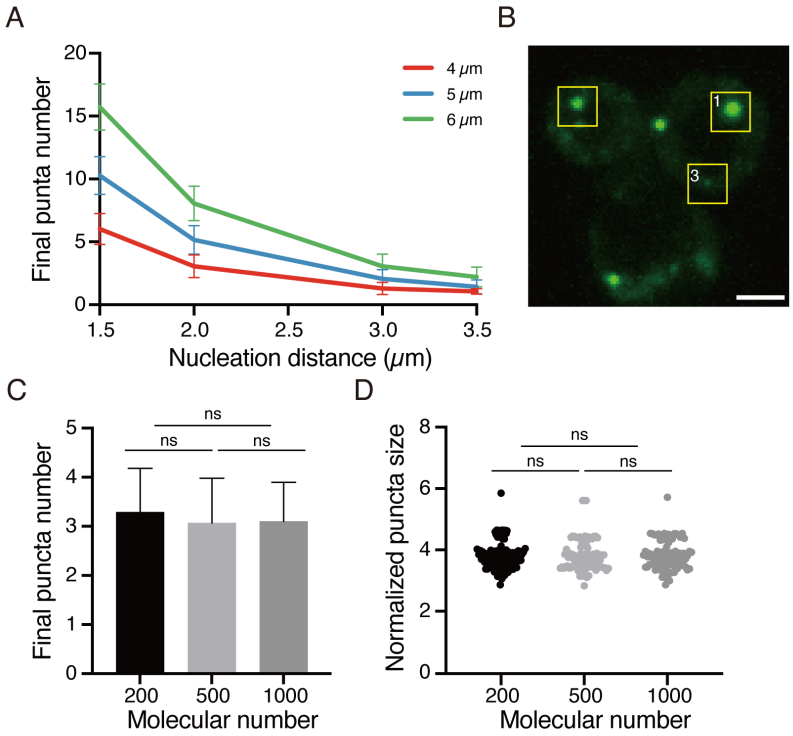

Supplementary Figure 3 | Effects of nucleation distance and molecular number on P-body formation simulation.

(A) Relationship between the final puncta number across different nucleation distances with different sizes of the cell.

(B) Representative images of the three P-body size classes. Yellow boxes highlight the representative P-bodies in the different size groups. 1 - large, 2 - medium, and 3 - small groups, respectively.

(C) Final puncta number is independent of molecular concentration in the nucleation simulation. The bar graph shows the final number of simulated P-bodies when varying the initial number of molecules (200, 500, 1000). Statistical significance was assessed by the Unpaired T-test (ns $P > 0.05$, $n = 200$ simulations per group).

(D) Puncta size distribution does not change upon molecular number. Statistical significance was assessed by the Unpaired T-test (ns $P > 0.05$, $n = 200$ simulations per group).